

# A Microcellular Ray-Tracing Propagation Model and Evaluation of its Narrow-Band and Wide-Band Predictions

Georgia E. Athanasiadou, Andrew R. Nix, and Joseph P. McGeehan

**Abstract**—Due to the site specific nature of microcellular operational environments, propagation models are required to take into account the exact position, orientation and electrical properties of individual buildings, and hence, ray tracing techniques have emerged as the dominant methods to predict propagation in such environments. A novel hybrid three-dimensional (3-D) ray tracing algorithm which can evaluate scenarios incorporating many thousands of objects by utilising the concept of “illumination zones,” is presented in this paper.

In order to evaluate the accuracy of the presented model, comparisons of narrow-band and wide-band predictions with measurements are performed for a variety of scenarios. First, power comparisons show that very accurate predictions can be achieved (rms errors less than 3.7 dB). Then, wide-band analysis shows that since the rms delay spread for systems with finite bandwidth is a function of the multipath phase, only average measured and predicted rms delay spread values can be compared and as a result, limited averaging can produce large rms errors. With sufficient averaging the achieved wide-band accuracy in terms of the predicted rms delay spread, is adequate for most planning purposes.

**Index Terms**—Narrow-band and wide-band radio channel measurements and predictions, propagation modeling, ray tracing.

## I. INTRODUCTION

IT IS A requirement for third generation mobile communications systems, such as UMTS/IMT2000, to be able to offer mobile access to voice, data and multimedia facilities in an extensive range of operational environments [1]. The need for planning these systems underlines the requirement for tools that will be able to provide the critical information to achieve this goal. Simple propagation models already play a critical role in the development, planning and deployment of mobile radio systems where coverage is the primary goal. However, with mobile telephony now being used by ever increasing percentages of the population, in most urban areas capacity is now replacing coverage as the most important issue. Since bandwidth is a scarce and very limited commodity, it follows that future mobile communication systems are most likely to operate in urban areas with cells that are far smaller than the present 1–2 km radii.

Manuscript received September 10, 1998; October 27, 1999. The work of G. E. Athanasiadou was supported by Nortel Networks, Harlow, U.K., during the second and third year of her Ph.D.

G. E. Athanasiadou was with the Centre for Communications Research, University of Bristol, Bristol, BS8 1UB, U.K. She is now with Adaptive Broadband Ltd., The Westbrook Centre, Block C1, Cambridge CB4 1YG, U.K. (e-mail: gathanasiadou@hotmail.com).

A. R. Nix and J. P. McGeehan are with the University of Bristol, Merchant Ventures Building, Bristol BS8 1UB, U.K.

Publisher Item Identifier S 0733-8716(00)01353-6.

Unlike previous large cell scenarios, in the case of small cells, statistical propagation models no longer provide acceptable results. Due to the site specific nature of the microcellular environments, propagation models are now required to take into account the exact position, orientation and electrical properties of individual buildings. Ray tracing produces deterministic channel models that operate by processing user-defined environments. In recent years, many authors have investigated the application of ray tracing to predict the amplitudes, time delays and arrival angles of the various multipath components for outdoor scenarios [2]–[11]. The diversity of information provided by these new simulation tools will enable researchers and designers to accurately predict the performance of wireless systems under a wide range of conditions [12].

In this paper a ray tracing algorithm is presented that allows the rapid generation of complex channel impulse response characteristics. The model makes full use of reflection, transmission and diffraction, and can evaluate scenarios incorporating many thousands of objects. Previous models have been two-dimensional (2-D) or three-dimensional (3-D) in nature; in this paper a hybrid technique is presented where the object database is held in two dimensions but the ray-tracing engine operates in three dimensions. The 3-D rays are produced by combining the results of two 2-D ray-tracers, one on the horizontal and one on the vertical plane. Moreover, by significantly enhancing the concept of “illumination zones” the performance of the algorithm has dramatically improved [11], [12].

The first part of this paper describes the ray-tracing model, with particular emphasis to the path generator that has been developed to simulate small cell propagation. The applicability of the model is demonstrated with results from a point analysis. In the second part, three sets of narrow-band and four sets of wide-band measurements are employed in order to evaluate the accuracy of the presented model and investigate propagation issues related with the validation of ray tracing results.

## II. THE RAY TRACING ALGORITHM

### A. The Propagation Model

Ray tracing is a technique based on *geometrical optics* (GO), an easily applied approximate method for estimating a high-frequency electromagnetic field [13]. GO assumes an infinite frequency for the propagating signal, and hence, the dissipating energy can be considered to be radiating in infinitesimally small tubes, often called *rays*. These rays are normal to the surfaces of equal signal power, lie in the direction of propagation and travel

in straight lines, provided that the refractive index is constant. In GO, only direct, reflected and refracted rays are considered, and consequently abrupt transition areas occur, corresponding to the boundaries of the regions where these rays exist. The *geometrical theory of diffraction* (GTD) [14] and its uniform extension, the *uniform GTD* (UTD) [15], [16] complement the GO theory by introducing a new type of rays, known as the diffracted rays. The purpose of these rays is to remove the field discontinuities and to introduce proper field corrections, especially in the zero field areas predicted by GO. The *Fermat principle* and the *principle of local field* are two basic concepts extensively used by the ray models [17]. The Fermat principle states that a ray follows the shortest path from a source point to a field point, while the principle of the local field states that the high frequency boundary processes, such as reflection, refraction and diffraction, depend only on the electrical and geometrical properties of the scatterer in the immediate neighborhood of the point of interaction.

In a wireless communications system, the signal arriving at the receiving antenna consists of several multipath components, each of which is the result of the interaction of the transmitted waves with the surrounding environment. The application of GO and UTD to a given propagation problem requires that the given configuration is decomposed into simple geometrical configurations for which the reflection, transmission and diffraction coefficients can be calculated. All rays contributing significantly to the channel characterization at the examined position must be traced, and the complex impulse response  $h(t)$  of the radio channel is then found as the sum of these contributions [18]

$$h(t) = \sum_{n=1}^N A_n \delta(t - \tau_n) \exp(-j\vartheta_n). \quad (1)$$

Here, the received signal  $h(t)$  is formed by  $N$  time delayed impulses (rays), each represented by an attenuated and phase-shifted version of the original transmitted impulse. The amplitude  $A_n$ , arrival time  $\tau_n$  and phase  $\vartheta_n$  of each ray are calculated using a combination of Snell's laws, UTD and Maxwell's equations [13]. Hence, according to the objects encountered by the  $i$ th ray, its complex received field amplitude  $E_i$  (V/m) is given by [19]

$$E_i = E_0 f_{ti} f_{ri} \left\{ \prod_j R_j \prod_k T_k \prod_l A_l(s', s) D_l \right\} \frac{e^{-jkd}}{d} \quad (2)$$

where

$E_0$	reference field;
$f_{ti}$ and $f_{ri}$	transmitting and receiving antenna field radiation patterns in the direction of the ray;
$R_j$	reflection coefficient for the $j$ th reflector;
$T_k$	wall transmission coefficient for the $k$ th transmission;
$D_l$	diffraction coefficient for the $l$ th diffracting wedge;
$e^{-jkd}$	propagation phase factor due to the path length $d$ ( $k = 2\pi/\lambda$ with $\lambda$ representing the wavelength).

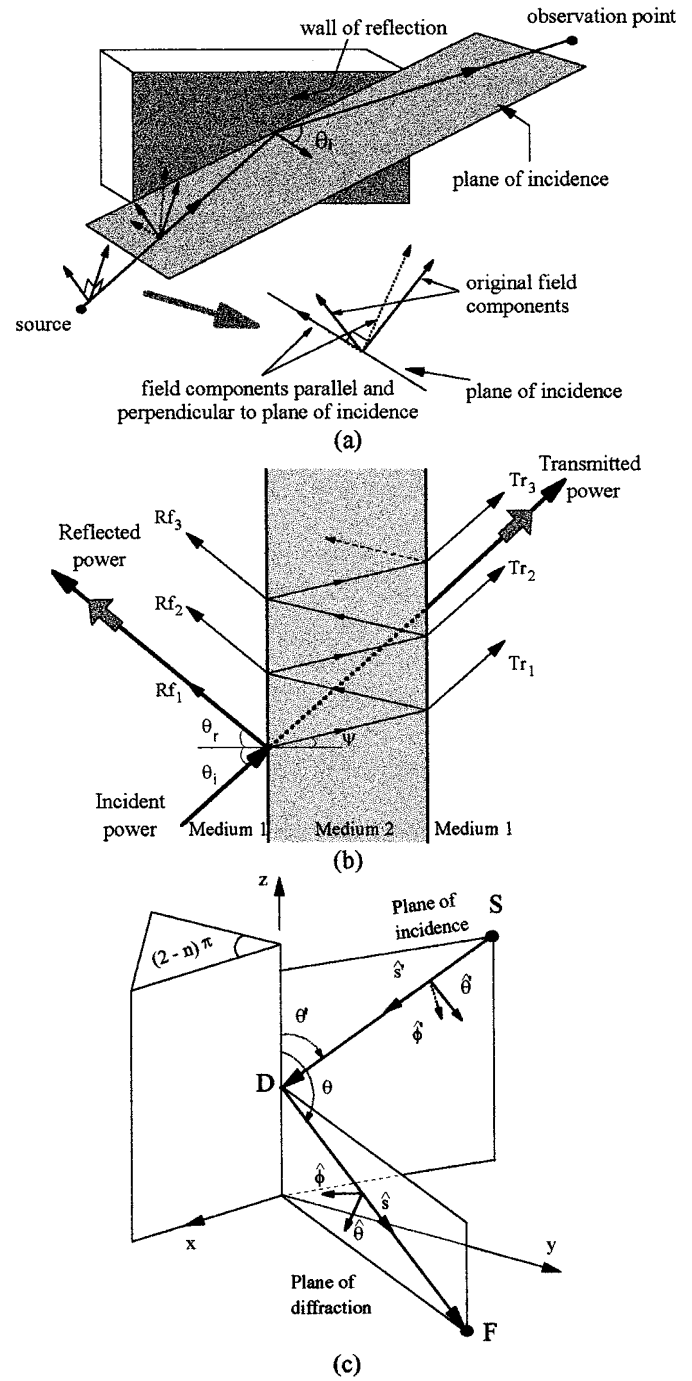


Fig. 1. Modeling the ray interactions with the simulated environment: (a) plane of incidence of a uniform wave incident at an oblique angle on an interface, (b) transmitted and reflected rays for an oblique incident wave on a conducting dielectric slab, and (c) ray fixed coordinate systems in the case of diffracted rays.

The diffraction coefficients are also multiplied by a factor  $A_l(s', s)$  which finds the correct spatial attenuation of the diffracted rays, given the  $1/d$  dependence in the last term. In the model, each wall is characterized by its permittivity, conductivity and thickness and all coefficients are functions of the angle of incidence and the object characteristics (Fig. 1).

An advantage of ray tracing models over other propagation models is the ability to incorporate antenna radiation patterns and particularly, as shown in (2), to consider the effect of the

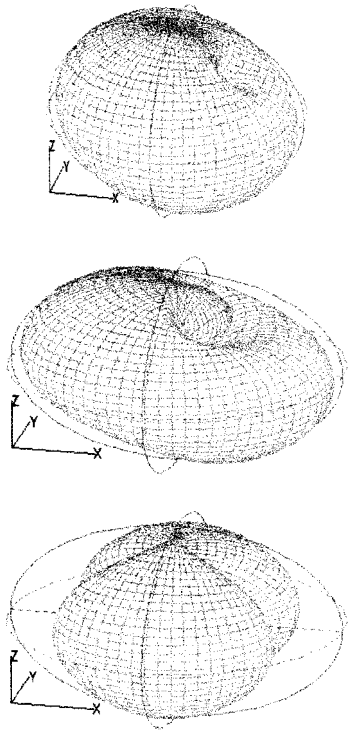


Fig. 2. Three dimensional radiation patterns (logarithmic scale) of: (a) the total power, (b) the power of the vertical ( $E_\theta$ ), and (c) the horizontal ( $E_\phi$ ) field components of the  $45^\circ$  tilted dipole, for the coordinate system of the model.

radiation pattern on each ray individually. Since in this model the geometry of each ray is examined in 3-D space, both the azimuth and elevation angles of arrival at the antennas are available, and hence, the model is capable of using 3-D radiation patterns. Moreover, in this model the antennas can be steered in any direction in space and hence, the channel can be examined for any antenna orientation. For example, Fig. 2 depicts the radiation pattern of a half wavelength dipole which is  $45^\circ$  tilted toward the  $x$  axis. Note that the model works with the electromagnetic field of the rays and hence, uses the radiation patterns of the field components. This feature, in conjunction with the fact that all reflections, transmissions, and diffractions are computed using 3-D vector mathematics, makes the model very useful in the study of different antenna polarizations and the examination of depolarization effects.

### B. The Path Generator

As previously explained, ray tracing represents electromagnetic waves as rays which are generated and launched in 3-D space from the transmitting antenna. In order to trace the ray paths, in this model a technique based on the electromagnetic theory of images [3], [5], [7], [8] has been developed. Rather than using the “ray launching” approach [6], [19] where rays are sent out at various angles and their paths are traced until a certain power threshold is reached, the technique adopted here considers all walls and obstacles as potential reflectors and evaluates the location of their base station images. This imaging technique works by generating an image table for each base station location, considering all the various wall reflection, trans-

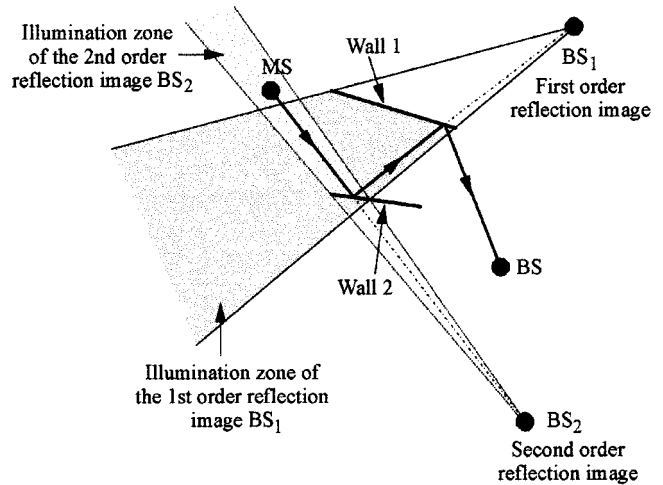


Fig. 3. Image generation and the illumination zones of the images: The basic concept and the path tracing using illumination zones.

mission and diffraction permutations that are possible in a given area. The image information is then stored and used to compute the channel characteristics at each mobile location. The use of such an image map dramatically improves the operating speed of the algorithm since repetitive calculations no longer have to be performed.

The basic concept of the image generation and the gradual build up of the image tree is extensively described in [3]. However, the algorithm used in this model has been dramatically enhanced with respect to the algorithm presented in [3]. One of the most significant improvements is the employment of an accurate “illumination zone,” which is the area for which an image can give a valid path (Fig. 3). Hence, in this model each image is associated with a specific illuminated area, which is also calculated and stored in the image table. This new information reduces the number of images and the time for path tracing significantly, and makes it feasible for the model to study large complicated environments and trace thousands of rays within a few seconds. Models like those presented in [7], [20] also employ similar methods in order to produce efficient algorithms.

With this technique, only walls and corners inside the illumination zone of the image can be used for the formation of new images, and moreover, these new images are not valid for the entire wall, but only for the part of the wall illuminated by the “parent” image. The illumination zones of high order reflection images tend to get narrower and this prevents the number of images increasing exponentially with the order of ray interactions with the environment. Hence in Fig. 3,  $BS_1$  can form a second-order reflection image ( $BS_2$ ) with only part of wall 2. Similarly, the diffraction corners give valid paths only for the exterior angle formed by the walls of the corner. In Fig. 4, because of the limited area covered by the illumination zone of image  $BS_1$ , all new images that can be produced from the walls and the diffraction corners of Buildings 2 and 3 are disregarded and only images from Building 4 are considered. Hence, the number of images is reduced dramatically since only images which are capable of producing valid paths are generated and stored in the image table.

Using illumination zones, the time for path tracing is reduced since the model has to search for valid paths among fewer images. An additional reason why this technique has considerably speeded up the ray-tracing algorithm is that the images that illuminate a mobile position can now be found very easily with a simple test. Hence, in order to find out whether an image can give a viable ray, instead of having to trace each possible ray all the way back to the base station, find the points of intersection with the corresponding walls and examine whether they are valid, the algorithm has only to check whether the mobile lies inside the illumination zone of the image. Once the above check with the last image of the path is completed, it is established whether a valid path exists and no further examinations for the rest of the images along the path are necessary. As a result, the model does not waste time tracing paths with many orders of reflection, only to find out at the last image that these paths cannot exist. For example, in Fig. 3, for the examined mobile position (MS), the image  $BS_2$  can give a valid path, while  $BS_1$  cannot, because the mobile is inside the illumination zone of  $BS_2$  and outside the zone of  $BS_1$ .

Previous models have been 2-D or 3-D in nature; in this paper a hybrid technique is presented where the object database is held in two dimensions but the ray-tracing engine operates in three dimensions. The model has been optimized for use in microcellular environments. The base station and the mobiles are assumed to remain below roof top height, where the signal is normally confined by local structures. As a result, the buildings are modeled as infinitely tall and the influence of roof-top diffraction is neglected. Building databases with arbitrary layouts can be employed, the walls are assumed to be vertical and the ground is assumed flat. Although the image generation is 2-D, the above assumptions allow the actual path tracing to be performed in three dimensions, as it shown in Fig. 5. First, horizontal ray tracing finds all possible paths in 2-D space. For each path found on the horizontal plane, ray tracing on the vertical plane takes place where the position of the ground reflection is calculated, and the height of each reflection or diffraction point both for the direct and the ground reflected ray is determined. Hence, for each path found in the image tree, an additional ray is created corresponding to its ground reflection. The combined results of the horizontal and vertical ray tracing produce 3-D rays.

To ensure as generic a model as possible, wall transmission and corner diffraction are fully supported even for onward propagating cases, i.e., each wall transmission or corner diffraction can undergo subsequent diffractions, reflections, and transmissions. The maximum number of allowable transmissions, reflections, and diffractions for each path is defined by the user. For microcellular studies, wall transmission is often ignored, however for determining in-building coverage this process needs to be considered.

### III. POINT ANALYSES DEMONSTRATING THE APPLICABILITY OF THE MODEL

In order to evaluate the applicability and to explore the variety of information that can be obtained from the ray tracing model,

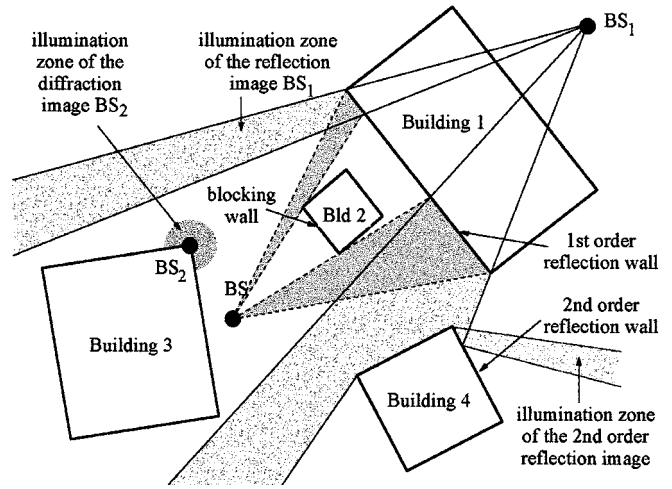


Fig. 4. Example which demonstrates the drastic reduction of the size of the image tree with the illumination zones (wall transmission is not considered here).

predictions are obtained in this section for the channel characteristics of a typical microcellular operational environment in central Bristol, U.K. The radio channel is examined at the points shown in Fig. 6, for a transmitting antenna (base station) placed at position "Tx." For ray tracing to be used in practical situations the model must be capable of importing standard commercially available building databases. In this study the building database has been extracted from the U.K. Ordnance Survey "Landline" database. The digital map was then preprocessed to remove any redundant information (e.g., internal walls) and diffraction corners were automatically added. The simulated area is approximately  $500 \times 500 \text{ m}^2$  and contains 438 external walls. All walls are modeled with smooth surfaces, a thickness of 0.6 m and the same electrical properties ( $\epsilon_r = 5$ ,  $\sigma = 0.005 \text{ Sm}^{-1}$ ) [19]. The base station and the mobile antennas are typical half wavelength vertically polarized dipoles, 5 and 1.57 m high, respectively. The carrier frequency is set at 1.823 GHz and the transmitted power is 30 dBm. For the results shown in this section, all rays are traced up to seven orders of reflection and one order of diffraction.

The model produces the complex channel impulse responses (Fig. 7), from which the received power,  $k$ -factor and the rms delay spread can be obtained. The elevation and azimuth angles of arrival at both antennas are also available (e.g., the azimuth angles of arrival at the base station are depicted in Fig. 8). Furthermore, to test and visualize the manner in which the power propagates in a specific scenario, figures such as Fig. 9, produced from the 3-D coordinates of the exact positions where the rays interact with the environment (i.e., points of reflections, transmissions, and diffractions) can be readily obtained. In these figures, it is also graphically illustrated how the algorithm exhaustively searches for all possible rays which reach the mobile inside the restrictions of maximum permitted interactions with the environment.

The first studied position, P1, is in a LOS area,  $\sim 55 \text{ m}$  away from the base station antenna. In the modeled impulse response, shown in Fig. 7(a), the LOS ray and the strong reflected rays from the surrounding buildings are evident. The received power

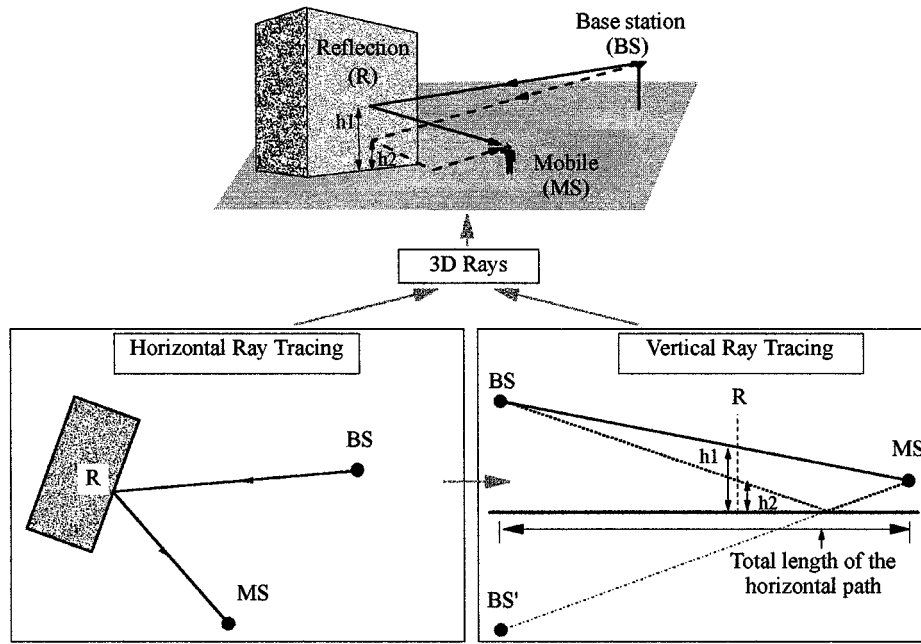


Fig. 5. 2-D/3-D hybrid analysis.

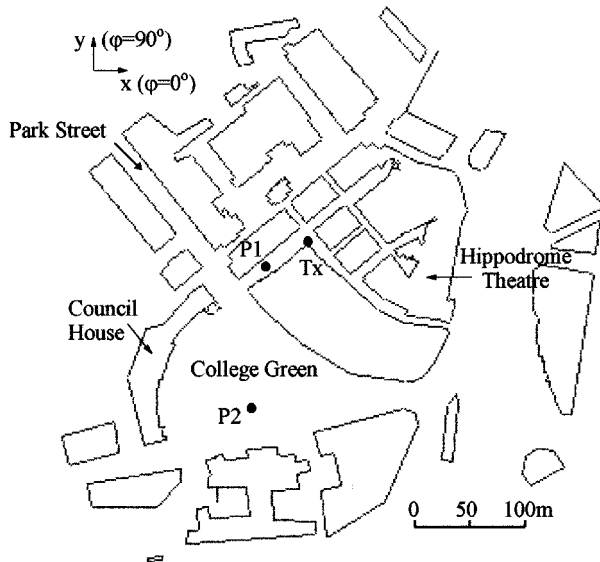


Fig. 6. Map of the microcellular environment under investigation.

is  $-32.96$  dBm, approximately 6 dB higher than the power of the LOS ray, since the strong reflected rays also contribute to the total signal level. However, due to these strong multipath rays, the  $k$ -factor at this position is relatively small for LOS conditions ( $-4.09$  dB). The rms delay spread, calculated within a 30-dB power window from the strongest ray of the power profile, is 43.92 ns. The power window is used in order to prevent long delayed rays raising significantly the rms delay spread values, when in reality they are too weak to impact the system's performance. In the power versus angle of arrival profile at the base station [Fig. 8(a)], the rays appear in pairs since two rays, the direct and the ground reflected paths, reach the antennas with the same azimuth angles. As expected, the strongest (LOS) ray is toward the direction of the mobile ( $\sim 210^\circ$ ) and most of the strong rays are reflections from the buildings on the sides of the

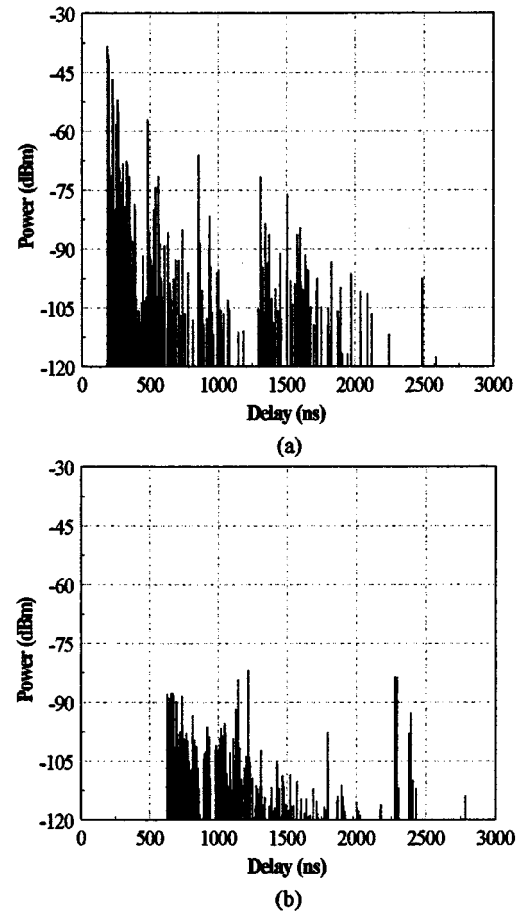


Fig. 7. Modeled impulse response at: (a) LOS point P1 and (b) NLOS point P2.

road, with similar angles of arrival. Nevertheless, not all energy comes from the direction of the mobile and strong reflections also exist in almost the opposite direction (at  $\sim 47^\circ$ ).

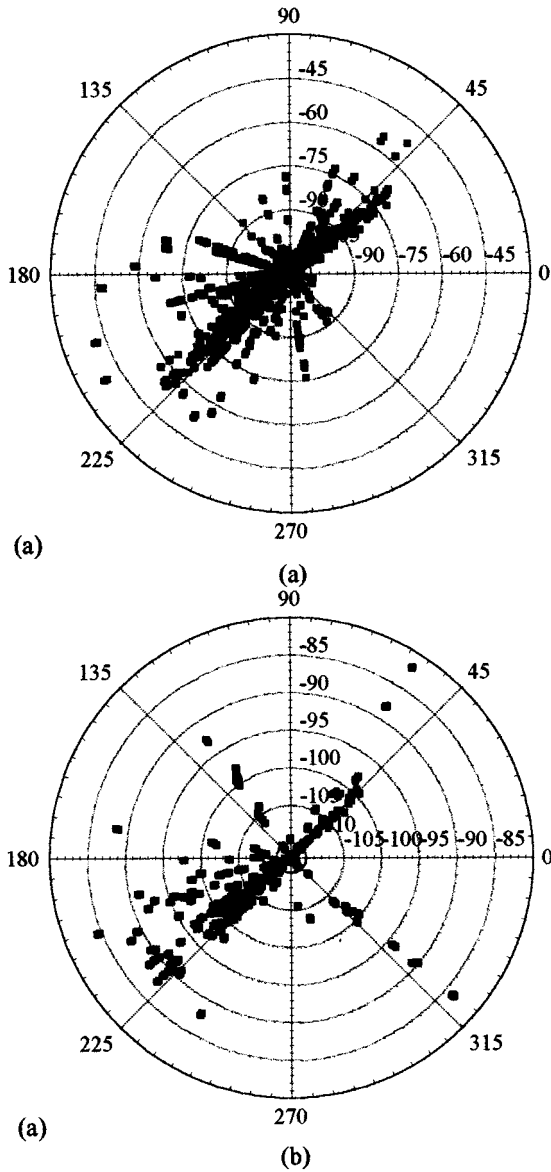


Fig. 8. Azimuth angles of arrival at the base station antenna at points: (a) P1 and (b) P2.

Unlike P1, point P2 is at a NLOS position in the open area of College Green, more than 155 m away from the base station (see Fig. 6). Generally, when LOS conditions do not exist, the channel characteristics become much more site dependent and hence, more difficult to describe with general rules. Because P2 is much further away from the base station than P1, there is higher power loss and hence, less rays reach this point (4676 rays with power greater than  $-150$  dBm are found for P1 and 2441 for P2). As shown in Fig. 7(b), the impulse response is no longer dominated by a few strong rays. Instead, a lot of rays with similar amplitudes reach the mobile, while the strongest ones arrive with considerable delay. Consequently, the rms delay spread at this point is high (624.59 ns) and the  $k$ -factor is considerably low ( $-12.41$  dB). Due to the significant contribution of all the relatively strong rays of the impulse response, the received power is  $-69.36$  dBm, approximately 13.5 dB higher than the power of the strongest ray. As illustrated in Fig. 8(b), most of the rays come from the direction of the corner between

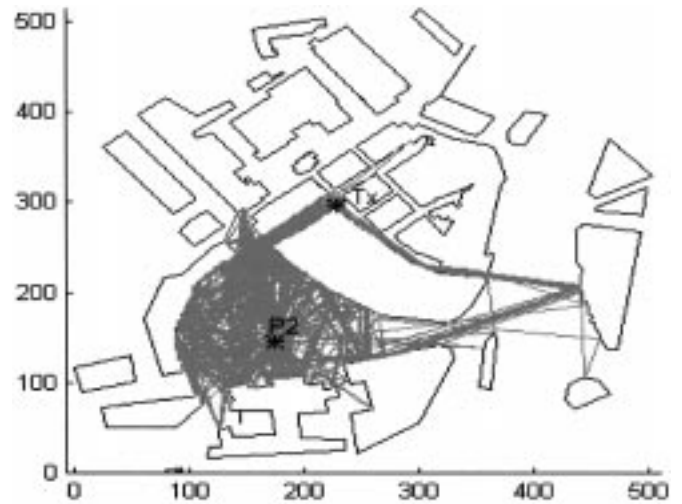


Fig. 9. Graphical display of the rays within the studied environment for position P2 (axes in meters).

Park Street and the street where the base station is located (at  $\sim 220^\circ$ ), as well as from reflections off the nearby buildings (see Fig. 9). Nevertheless, the strongest rays reach the mobile after being reflected off the building on the right of the base station (at  $\sim 57^\circ$ ) or travelling around the building between the two antennas, following a longer path (at  $\sim 320^\circ$ ).

#### IV. EVALUATION OF THE NARROW-BAND AND WIDE-BAND PREDICTIONS OF THE MICROCELLULAR MODEL BY COMPARISON WITH MEASUREMENTS

In this section the validity of the ray tracing model is investigated. Evidence for the accuracy of the model is provided through comparisons of the predictions with three sets of narrow-band and four sets of wide-band measurements. The evaluations are performed for both LOS and NLOS positions. The difficulties encountered when comparing predicted with measured channel characteristics are also discussed.

##### A. Comparison of Predictions with narrow-band Measurements

Power predictions are compared here with narrow-band measurements taken in central Bristol, U.K. The field trials were performed under the British Telecom (BT) Virtual University Research Initiative (VURI) project [21]. The measurement site is that described in Section III and depicted in Fig. 6. The examined transmitter positions and the test route are depicted in Fig. 10. The antennas were both below the roof height of adjacent buildings, with the transmitting antenna mounted on a mast at a height of 5 m above the ground level. The transmitted power was 30 dBm (including the cable and antenna losses) at 1.823 GHz. Typical half wavelength vertically polarized dipoles were used at both ends of the radio link. The receiver was at a height of 1.57 m, mounted on a trolley which was slowly and carefully moved along the predefined route shown in Fig. 10. The trolley was chosen, instead of the more convenient option of a car, in order to maximize the accuracy of the mapping of the measurement results to actual positions, which is critical when validating site specific models. The narrow-band receiver recorded field

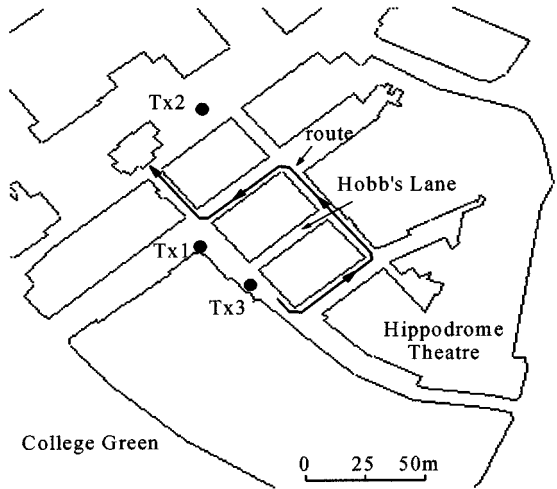


Fig. 10. Microcellular map of the measurement area.

strength against distance from the starting point, with a spatial sampling rate of 4 cm. The fast fading was extracted from the measured results with a sliding rectangular window averaging process. A 10-wavelength window (equivalent to 1.67 m) was chosen, so that the measurements maintain their site specific information as much as possible.

The model's performance is evaluated under NLOS, as well as LOS conditions. Most importantly, the route includes deep shadow areas where energy can reach only through multiple reflected and diffracted rays. Field trials were carried out along the same route for three different transmitter positions. For each transmitter location, several measurement runs (3–6) were performed along the same route and with the same configuration. For more representative results, and in order to remove localized temporal effects, the slow fading envelopes were averaged to produce a mean envelope. The evaluation of the model is performed by comparison of the mean measurement with predicted results. From the different measured results it was noticed that there was a high degree of correlation between the various runs, although some of them were taken on different days [21]. The rms error<sup>1</sup> of each of the measured envelopes with respect to the mean envelope is as high as 3.45 dB and the total rms error is 2.69 dB. This is a measure of the repeatability of the measurements. Since it is not reasonable to expect the prediction tools to reproduce the measurements with more accuracy than their own repeatability, this value sets the upper limit of attainable accuracy of a propagation model.

The configuration of the model was the same as in Section III. Unlike the field trials, the spatial resolution between the prediction points was 0.5 m. This is because the predicted received power, which is produced as the sum of the power of the rays reaching the receiver, is inherently time averaged and no further action is needed in order to remove the fast fading. For the results shown here, all rays are traced up to nine orders of reflection and two orders of diffraction. All predictions were obtained employing the same simulation parameters.

<sup>1</sup>The rms error between the  $N$  values of  $\alpha_i$  and  $b_i$  is:  $\text{rms\_error} = \sqrt{1/N \sum_{i=1}^N (\alpha_i - b_i)^2}$ . The rms error equals the square root of the sum of the squares of the mean error and the standard deviation and is often used as a more representative measure of error.

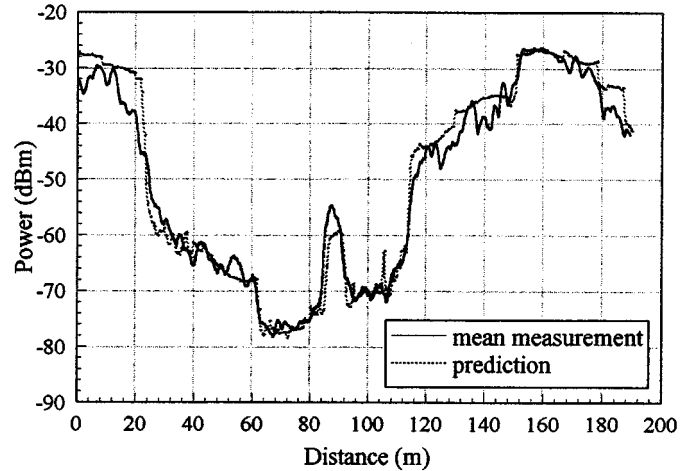


Fig. 11. Model's prediction against mean measurement for transmitter position Tx1.

In order to analyze the inherent discrepancies that result from the limited averaging of the measurements along the test route, predictions were also obtained by producing slow fading envelopes similar to those measured. This second set of predictions was produced from the model by emulating the measurement process. From the complex channel impulse responses, the "instantaneous" power was produced every 4 cm. At each point, the summation of the vectors of the electric field of all the rays reaching the receiver produces the total field strength from which the power prediction derives. The predictions obtained in this manner are equivalent to the raw data of a measurement run. Following the averaging process used for the measurements, a 10-wavelength sliding window was used to remove the fast fading and produce a predicted slow fading envelope. Four such envelopes are produced with this method. Because of the completely static environment of a ray tracing model, for each new envelope the route is offset by a distance of 0.3 m in a random direction (the same for all points) in order to produce a different envelope. Alternatively, random phases could be used, but the spatial offsets were preferred in order to reduce the receiver position uncertainty. The slow fading envelopes were then averaged to produce a mean predicted envelope similar to the measured envelope.

*1) Comparison Between Measurements and Predictions for Transmitter Tx1:* Fig. 11 depicts the mean measurement and the predictions of the model for the first transmitter position, Tx1. At the beginning of the route the receiver is at a LOS position about 50 m away from the transmitter. As it turns left and moves into NLOS positions, the mean signal level decreases significantly (more than 20 dB, at ~20 m). A further drop (less than 10 dB, at ~60 m) is evident as the receiver turns into the second corner and enters a deep shadow region. An increase of at least 18 dB in power (~86 m) is due to the movement of the receiver along the end of Hobb's Lane (see Fig. 10) which acts as a street canyon for the transmitted electromagnetic waves. As the receiver reenters the deep shadow area, the power falls again, however higher signal levels are measured since the distance between the two antennas is reduced. When the receiver turns left and enters less shadowed areas (~118 m), the signal increases by about 15 dB and keeps increasing as the trolley ap-

TABLE I  
ERRORS FOR THE COMPARISON BETWEEN  
THE PREDICTIONS AND THE MEASURED RESULTS

	Mean error (dB)	Standard deviation (dB)	RMS error (dB)
Tx1 predictions	1.0718	3.2011	3.3718
Tx1 predictions with average samples	1.1376	2.9027	3.1174
Tx2 predictions	-0.0276	3.3170	3.3127
Tx3 predictions	-0.0610	3.7093	3.7048

proaches the second LOS section of the route. The transition from NLOS to LOS (~157 m) is not as dramatic (approximately 10 dB increase) because the two antennas are already very close and strong reflections have raised the mean signal strength. The measured power falls slowly as the receiver moves away from the transmitter and finally reenters a NLOS area near the end of the route. Obviously, because the power changes are site dependent, there is no simple rule for the degree of variation of the signal level as the receiver moves into or out of LOS, NLOS, or deep shadow areas. The simulation results agree very well with the measurement trend throughout the route, remaining within a few dB from the mean measurement for the majority of the receiver positions. The mean difference between the predictions and the measurements, calculated with both values in a logarithmic scale, is 1.07 dB with an rms error of 3.37 dB (see Table I).

Fig. 12 shows results for the comparison between measurements and predictions emulating the measurement process for transmitter Tx1. Because of the limited averaging, the mean prediction produced by averaging the simulated envelopes varies more than the results calculated from the summation of the powers of the rays (shown in Fig. 11). Although the two predictions are close for the majority of the points, their difference indicates that the averaging of the results of the model emulating the measurement process is still not complete, since it is confined along the route direction. On the other hand, because each envelope point derives from spatial averaging along ten wavelengths, the predicted envelopes, like the measurements, do not present sudden peaks similar to those appearing at the point prediction (e.g., see Figs. 11 and 12 at ~105 m). The prediction from the average simulated envelopes fluctuates around the predictions from the summation of the ray powers and hence, their mean difference is just -0.072 dB but with an rms error of 2.16 dB. Moreover, the predicted envelopes do not show the variability of the measurements because of the completely static and simplified simulated environment. As a result, the total rms error produced from the comparison between each of the predicted envelopes and the mean envelope, is smaller than that of the measured envelopes (1.88 and 2.69 dB, respectively).

Although there is only a small difference between the model's predictions with the two different averaging methods, the prediction with the averaged samples keeps better track of the mean measurement, as shown in Fig. 12. Furthermore, the fluctua-

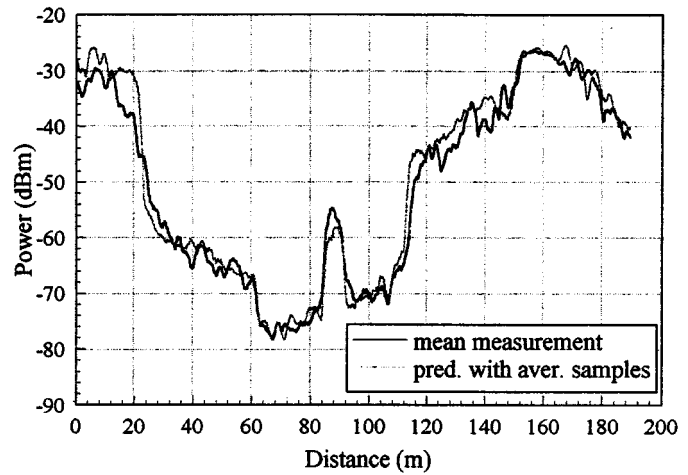


Fig. 12. Model's prediction produced with averaged samples and the mean measurement for transmitter position Tx1.

tions of the mean simulated envelope are very similar to those of the measured envelope. This behavior is reasonable and expected since the same sampling and averaging process is used for the measurements and the predictions with averaged samples. Nevertheless this prediction method was only employed here for comparison purposes and it must be stressed that the power results from the summation of the powers of the rays is the ultimate averaging method both from a theoretical [23] and practical [24] point of view. The error statistics are slightly better for the prediction with the averaged samples than with the prediction of the summation of the power of the rays. The mean and rms errors are 1.13 and 3.11 dB, respectively.

As seen in Figs. 11 and 12, when the receiver turns into the first corner, at about 20 m from the route start, the transition from the LOS to NLOS area is more abrupt for the simulation results rather than the measurements. It is believed that missing scatterers in the database caused this divergence. For example, large lorries which were parked at the back of the Hippodrome Theatre (see Fig. 10) during some of the measurements were completely ignored. These lorries affected the measured envelopes and as a result, smoother transition from LOS to NLOS conditions occurred (between 15 and 30 m in Figs. 11 and 12).

2) *Comparison Between Measurements and Predictions for Transmitter Tx2:* As shown in Fig. 10, the second transmitter position, Tx2, is outside the immediate area of the measurement route with LOS only along the last 1 m of the route. This location was chosen in order to ensure that a large portion of the route is in the shadow region with respect to the transmitter. For this position, three measurement runs were performed and as for the first transmitter location, the mean measurement was calculated (Fig. 13). During the first 50 m of the route the received signal level is relatively low since there are three buildings between the two antennas. As the trolley turns into the second corner the received power increases by more than 20 dB (~60 m), as rays can now easily reach the receiver by travelling along the road which acts as a waveguide. A significant decrease in signal power (about 25 dB) is caused as the receiver turns into the third corner, (~118 m). Although the received power increases by about 10 dB as the receiver turns into the last corner (~157 m), the signal remains low as long as the trolley is be-



hind the building and only at the last section of the route, as the receiver approaches the LOS area, does the signal level start increasing again. As shown in Fig. 13, despite the difficulty of this route, which lies almost entirely in the NLOS area, the model manages to keep very good track of the measurements even in deep shadow areas away from the transmitter. The mean error is  $-0.02$  dB with an rms error of 3.31 dB.

3) *Comparison Between Measurements and Predictions for Transmitter Tx3:* The third transmitter location, Tx3, is the one closest to the measurement route. Fig. 14 depicts the mean measurement produced from the four measurement runs performed. The shape of the measured envelope is similar to the measured envelope for Tx1, however with different power levels. During the first LOS section of the route, the measured power is about 10 dB higher than for Tx1. As the receiver enters the NLOS region, the signal falls significantly, more than 20 dB. Unlike when the transmitter was at position Tx1, as the receiver turns around the second corner, the power level does not change dramatically because strong reflected and diffracted rays can still reach the receiver travelling around the building between the two antennas. As the power starts to fall, strong rays come from Hobb's Lane and the received power increases by more than 25 dB. When the trolley passes the crossing with Hobb's Lane, the power falls again and remains low for the rest of the NLOS section of the route. The receiver reenters the LOS area after the last corner, where the received power rises sharply.

The model's predictions were obtained using exactly the same simulation parameters as for Tx1 and Tx2. Again, the model manages to follow the measurements very closely for the majority of the receiver positions. The correct power levels have been predicted for the LOS and most of the NLOS sections of the route. The only deviation exists for the section of the route between the first and second corner. This area is at the back of the Hippodrome Theatre and a possible explanation for the errors in this area may be some missing scatterers in the data base (see Section IV-A1). Nevertheless, the problem is confined in a small region and the model follows the trend of the measurements for the rest of the route. The mean error is  $-0.06$  dB with an rms error of 3.70 dB.

### B. Comparison of Predictions with Wide-Band Measurements

In this section, predictions from the microcellular model are compared with results from wide-band measurements. Data from two different measurement campaigns are used. The first campaign took place in Bristol and the second at BT Labs, Martlesham, Suffolk, U.K. The measurements were performed with correlation sounders. The impulse response obtained from a ray tracing model corresponds to measurements made with infinite bandwidth (i.e., each received ray corresponding to a perfect impulse in the time domain). To be able to compare simulated results with actual measurements, the predicted impulse responses are convolved with the autocorrelation of the pseudonoise (PN) sequence used in the measurement system. The output of the convolution represents the power delay profile as seen at the resolution of the measurement hardware.

1) *Comparison Between Predictions and Wide-Band Measurements Performed in Bristol (Park Street):* Fig. 15 depicts the building database of the area where the first measurement

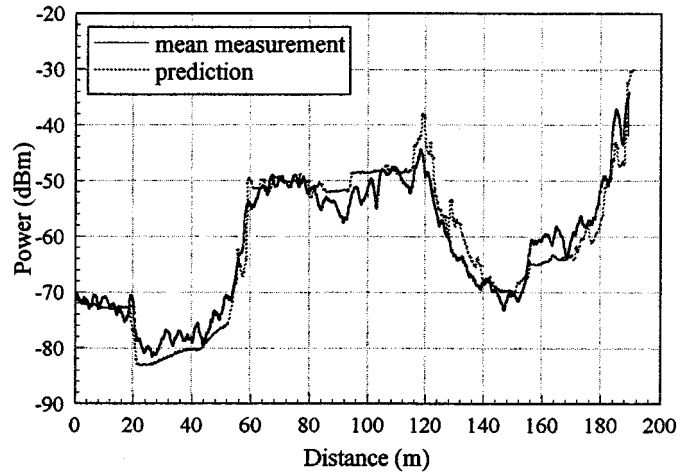


Fig. 13. Model's prediction against mean measurement for transmitter position Tx2.

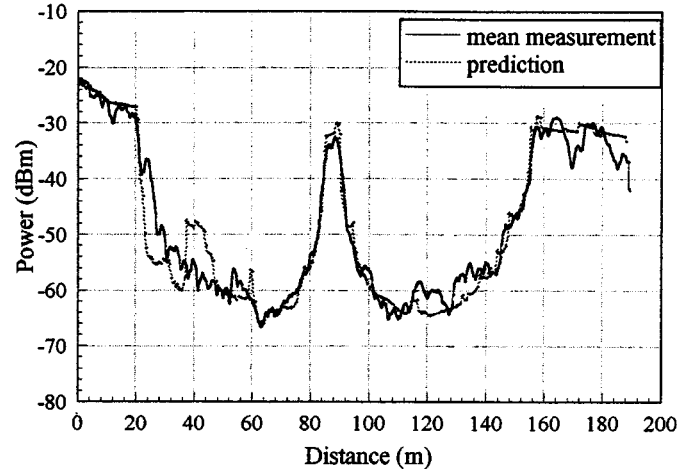


Fig. 14. Model's prediction against mean measurement for transmitter position Tx3.

campaign was performed. The modeled region is 700 by 800 m and includes the Engineering Buildings of the University of Bristol, Park Street and the College Green area, where the transmitter was located. The simulated and measured results were obtained at a frequency of 1.834 GHz. The transmitting and receiving antennas were vertical dipoles placed at heights of 3 and 1.5 m, respectively, and the transmitted power was 20 dBm. The receiver was mounted on a car and recorded the channel impulse response approximately every 50 cm. The sounder used for the field trials [25] employed a 511-bit-long PN sequence clocked at 8 MHz. In the model, the buildings were characterized by a single set of electrical properties ( $\epsilon_r = 5$ ,  $\sigma = 0.005$  S/m) and the walls were assumed smooth and to have 0.4 m thickness. For the results shown below, all rays were traced up to seven orders of reflection and one order of diffraction. The measurements were taken along the 195-m-long test route indicated in Fig. 15. The route starts toward the end of Park Street, passes in front of the transmitter (at  $\sim 65$  m) and enters the open area of College Green.

Fig. 16 shows a typical power delay profile produced from the propagation model for a receiver position approximately 45 m away from the starting point of the route. In addition to showing

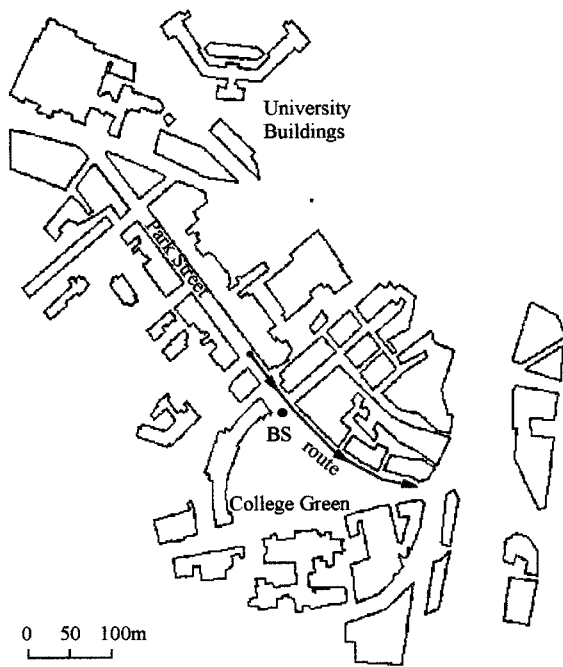


Fig. 15. Microcellular map and test route for the wide-band measurements.

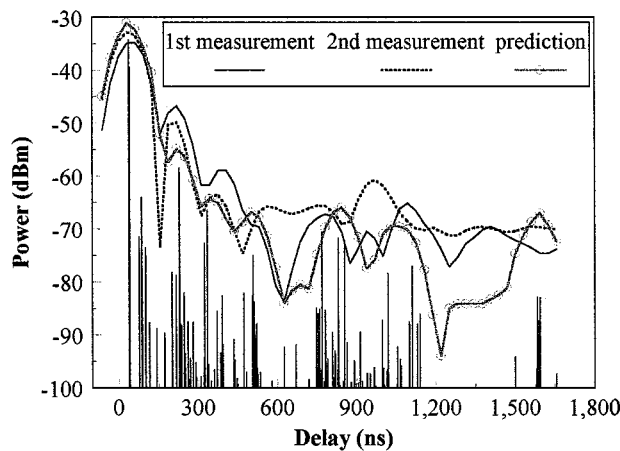


Fig. 16. Measured and modeled delay profiles.

individual rays at infinite resolution, the graph also shows the simulated impulse response taking into account the resolution of the 8-MHz channel. The two measured profiles at this point are also shown in Fig. 16, with the second measurement taken several minutes after the first. Although these three power profiles have similar shapes, this level of agreement is not seen at all points in the simulated route. In practice, the use of a finite bandwidth in the channel sounder introduces some variability into the measured delay profile. For example, using an 8-MHz PN-based sounder, the chip duration is 125 ns. This limited time resolution results in the addition of the multipath rays arriving at similar times. Hence, the resulting power delay profile at any time  $\tau$  is generated from the vector summation of all multipath components within the time resolution of the sounder. The actual profile shape (and hence the rms delay spread) is therefore a function of the phase of many individual arriving rays. This phenomenon is shown graphically in Fig. 17 where the same modeled profile at infinite resolution has been processed

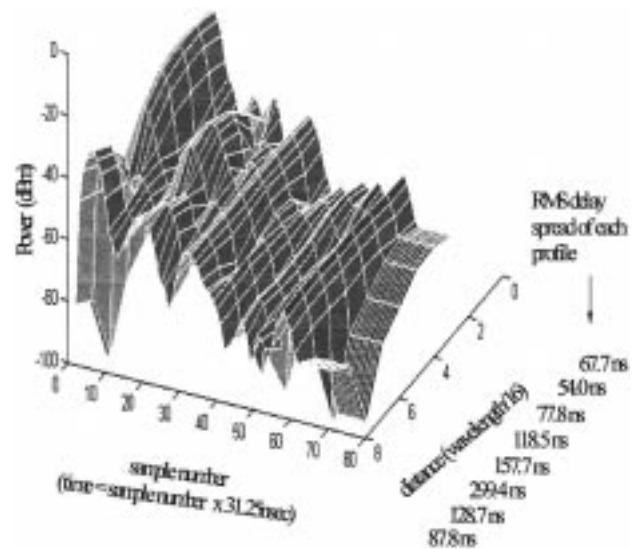


Fig. 17. Finite bandwidth profile variation.

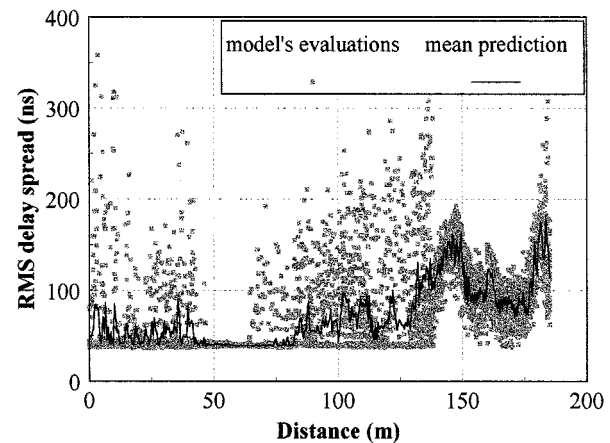


Fig. 18. Average and instantaneous predicted dispersion.

to an 8 MHz bandwidth at half wavelength intervals. The resulting “finite bandwidth” profiles differ significantly in both their shape and rms delay spread. The rms delay spread varies from as low as 54 ns to as high as 289 ns (a 20-dB power window is used for these calculations in order to stay above the noise floor of the sounder). For comparison, the original infinite bandwidth profile has an rms delay spread of 90 ns, the mean simulated rms delay spread was 122 ns while the measured value is 125 ns. It is clear from these observations that since the arrival phase of each ray varies significantly with distance and cannot be accurately predicted, it will be almost impossible to achieve agreement in either the instantaneous measured profile shape or the value of rms delay spread for a single individual measurement. As with the narrow-band measurements, the comparison between measured and modeled results should be for average values in a small area around the examined mobile position.

Fig. 18 shows the modeled instantaneous rms delay spread variations calculated for the parameters employed by the sounder. At each point the rms delay spread was calculated for 16 profiles spaced at half wavelength intervals. The plot shows significant fluctuations of the rms delay spread values. The

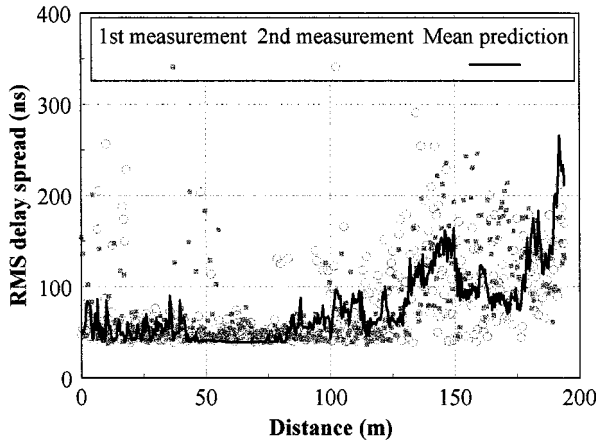


Fig. 19. Measured and simulated rms delay spread.

actual variation is a function of the receiver bandwidth. For each location, the 16 instantaneous values have been processed to generate the average rms delay spread. Fig. 19 shows two sets of measured rms delay spread results, for the route indicated in Fig. 15. The second set of measurements was taken at the same location and for the same test route but several minutes later. Similar to the simulated results, each set of measured rms delay spreads shows considerable variability from point to point. Furthermore, there are several disagreements between these two sets of measurements and the rms difference between them is 54.83 ns. Most validation studies assume the measured data to be “correct” and attribute all errors to the modeling process. Nevertheless, as shown in the measurements presented here, in reality there would be significant variations in measured data taken consecutively at the same location. It is not reasonable to expect propagation models to produce better agreement than that obtained between identical measurements in the same location. Only repeatable characteristics of the radio channel can be predicted as mentioned before and hence, in the case of wide-band results the only feasible comparison is between average measured and simulated values.

Fig. 19 also depicts the average simulated rms delay spread calculated from 16 profiles spaced at half wavelength intervals (as shown in Fig. 18). The average “finite bandwidth” predicted values varies above and below the measured data. The mean measured rms delay spread for the whole route is 82.04 ns while the mean predicted value is 76.68 ns. The rms difference between the average predicted values and the mean of the two measurements is 34.38 ns. Since only two measurement sets were available, in order to remove the bias and get more reliable results, more averaging was used. In Fig. 20 the rms delay spread measured values are calculated for the positions between two points by averaging the measured values of the adjacent positions (i.e., at each point the mean value of 4 measured values is obtained, 2 from each adjacent receiver position). Now that the measured results are more averaged, it becomes obvious that the predictions tend to follow the measurements for the majority of the route positions (the rms difference between the average predicted and measured values is now 29.11 ns).

2) *Comparison Between Predictions and Measurements Performed at the BT Labs:* Wide-band predictions from the micro-

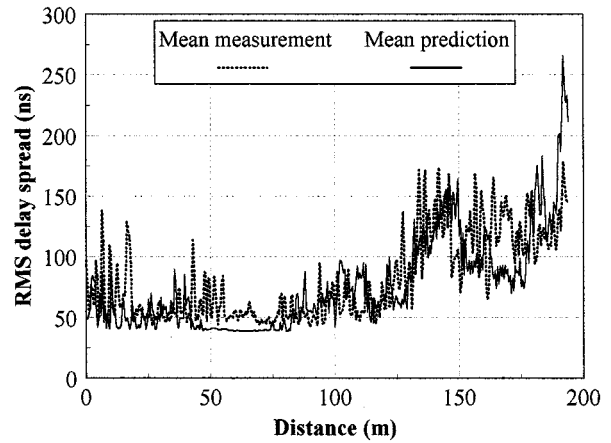


Fig. 20. Mean measured and predicted rms delay spread along the route.

cellular model are compared in this section with results from three sets of wide-band measurements performed and presented by M. C. Lawton in [3]. The measurements were taken with a correlation sounder built by BT, using a 255 bit PN sequence with 20-Mb/s clock rate and 100-ns full pulsewidth. The measured dynamic range of the sounder was 31 dB. The heights of the transmitting and receiving antennas were 2.5 and 1.5 m, respectively, well below the heights of the surrounding buildings. Vertically polarized dipole antennas were used and the carrier frequency was set at 1.823 GHz. The simulated building database of the area extracted manually from a map is depicted in Fig. 21. In the model, the walls are characterized with the same set of parameters ( $\epsilon_r = 5$ ,  $\sigma = 0.005$  S/m, and 50 cm width).

As the receiver was moved along the routes shown in the Fig. 21, the power profile of the radio channel was measured every 10 m. As explained before, because of the limited bandwidth of the sounder, the power profile at each point is highly variable. For this reason, a large number of snapshots (~300) were measured at each receiver position and the mean rms delay spread was calculated. However, the snapshots were taken for exactly the same receiver position with variations occurring only due to the temporal nature of the environment, resulting in limited averaging of the measurements. As with the previous comparisons, the channel dispersion predictions were obtained from the model after emulating the finite bandwidth and the system characteristics of the measurement equipment. At each receiver position, the average rms delay spread is calculated from 16 profiles spaced at half wavelength intervals. In order to illustrate the variability of the results, the evaluations of the model are displayed every 0.5 m, together with the minimum and maximum predicted value at each position.

The first route (Route 1 in Fig. 21) is in the LOS area. Initially the receiver is approximately 10 m away from the transmitter and gradually moves away. As shown in Fig. 22, the mean predicted results follow the measured rms delay spread closely. The mean error is 7.6 ns with an rms error of 10.2 ns (Table II). The second route (Route 2) lies entirely in the NLOS area. As depicted in Fig. 23, the measured values along this route are almost double the values of the first route. The rms delay spread is generally higher along this route, since there is not a dominant LOS ray in the power profiles, while the rays

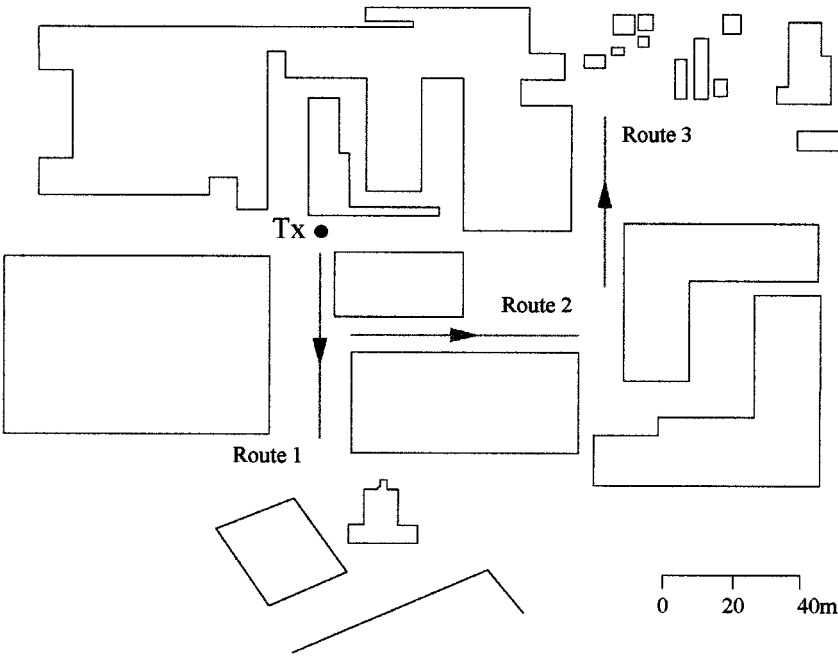


Fig. 21. Microcellular map of the second site of wide-band measurements.

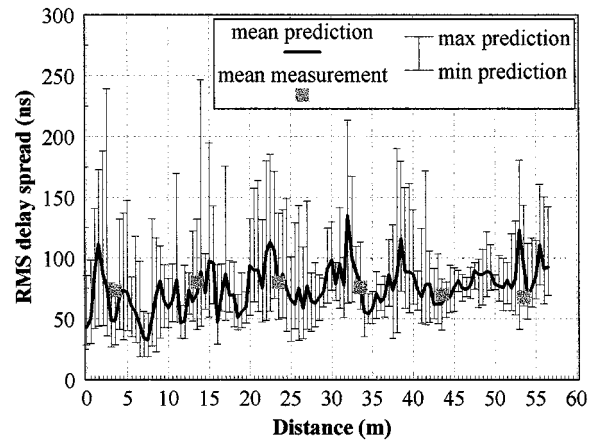


Fig. 22. Predictions and measurements along the first route.

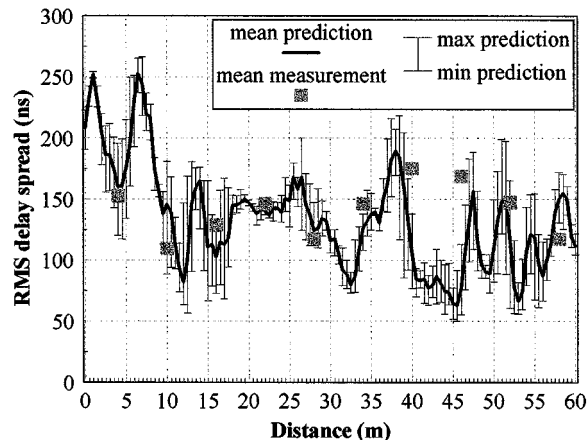


Fig. 23. Predictions and measurements along the second route.

TABLE II

ERRORS STATISTICS OF THE COMPARISON BETWEEN MEASURED AND PREDICTED rms DELAY SPREAD RESULTS ALONG THE THREE MEASUREMENT ROUTES

	Mean error (nsec)	Standard deviation (nsec)	RMS error (nsec)
Route 1	7.6	6.8	10.2
Route 2	27.1	31.2	41.3
Route 3	27.4	18.1	32.8

can reach the receiver following many different paths with various lengths. The mean and rms error of the evaluations of the model with respect to the measured values is 27.1 and 41.3 ns, respectively. Finally, the third route (Route 3) is even further from the transmitter. A small section of the route is under LOS conditions, but generally the route is in the NLOS area, with rays having to pass through narrow gaps through buildings or

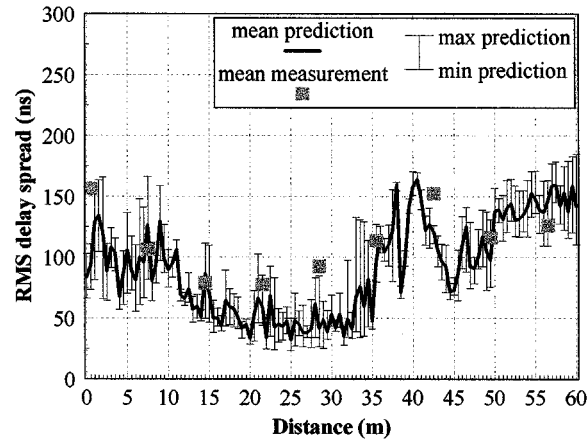


Fig. 24. Predictions and measurements along the third route.

travel around them following long paths to reach the receiver (see Fig. 21). As shown in Fig. 24, the simulated and measured

values follow the same trend, although the predicted values are generally lower (mainly because distant scatterers are not included in the building database). The mean and rms prediction errors for this route are 27.4 and 32.8 ns, respectively. Given the inaccuracies of the building database and the limited information on the measurement conditions, the errors are considered relatively low.

The variability of the predictions along the first route (Route 1) is significant in spite of the LOS conditions. The values vary from as low as 25 ns, to as high as 250 ns. In comparison with the rms delay spread values along the second and third route (Figs. 23 and 24, respectively), it seems that although the mean values are generally lower, the values fluctuate more in LOS areas rather than under NLOS conditions. Along the first route all rays are relatively strong and consequently the power delay profile fluctuates severely as the phases of the rays in the same time bin change. Since the full pulsewidth is 100 ns, rays with path lengths which differ by up to 30 m, add up vectorially to form the value of the impulse response of the channel for a specific delay. The path length of the LOS ray does not differ a lot from the path length of the first order reflections from the nearby buildings (see Fig. 21), resulting in highly variable channel dispersion values.

## V. DISCUSSION—CONCLUSION

This paper has presented a novel site specific urban propagation model suitable for microcellular operational environments. Employing a hybrid technique, an algorithm was developed where the ray-tracing engine operates in three dimensions, by combining the results of two 2-D ray-tracers, one for the horizontal and one for the vertical plane. Moreover, except for the position of each image, the exact area for which this image is valid is also calculated and stored in the image map. The employment of accurate "illumination zones" dramatically enhances the performance of the model.

In order to evaluate the accuracy of the outdoor model, comparisons of wide-band and narrow-band predictions with measurements were performed for a variety of scenarios. The power predictions were evaluated for three different transmitter positions in a typical urban environment. The predictions followed the trend of the measurements closely even in deep shadow areas. The mean errors were less than 1.1 dB and the rms errors did not exceed 3.7 dB. Predictions emulating the measurement process showed that deviations between measured and simulated results can exist due to limited averaging of the measurements.

The outdoor wide-band analysis revealed that attention must be paid when comparing predicted and measured wide-band results, because the rms delay spread for systems with finite bandwidth is a function of the multipath phase and varies significantly at distances separated by fractions of a wavelength. In practice only average measured and predicted rms delay spread values can be compared and as a result, limited averaging can produce large rms errors (results from Park Street). The rms errors from a second measurement campaign with more averaging (BT Labs) were around 10 ns for LOS and 32 and 40 ns for NLOS scenarios. In all cases, the mean prediction error was less

than 10% of the mean measurement in LOS and 24% in NLOS cases.

## ACKNOWLEDGMENT

The authors would like to thank Dr. G. V. Tsoulos for significant contribution to this paper through many technical discussions and useful suggestions. They also thank Dr. M. C. Lawton for the provision of the wide-band measurements at the BT Labs, Dr. C. M. Simmonds for the wide-band measurements in Park Street, Bristol, and Dr. S. A. Meade, Mr. E. K. Tameh, together with the BT VURI team for the narrow-band measurements.

## REFERENCES

- [1] J. Rapeli, "UMTS: Targets, system concept, and standardization in a global framework," *IEEE Personal Commun.*, vol. 2, no. 1, pp. 20–28, Feb. 1995.
- [2] K. J. Gladstone and J. P. McGeehan, "Computer simulation of multipath fading in the land mobile radio environment," *Proc. Inst. Elect. Eng.*, pt. G, vol. 27, no. 6, pp. 323–330, Dec. 1980.
- [3] M. C. Lawton and J. P. McGeehan, "The application of a deterministic ray launching algorithm for the prediction of radio channel characteristics in small—Cell environments," *IEEE Trans. Veh. Technol.*, vol. 43, pp. 955–969, Nov. 1994.
- [4] S. Y. Tan and H. S. Tan, "UTD propagation model in an urban street scene for microcellular communications," *IEEE Trans. Electromag. Compat.*, vol. 35, pp. 423–428, Nov. 1993.
- [5] U. Dersch and E. Zollinger, "Propagation mechanisms in microcell and indoor environments," *IEEE Trans. Veh. Technol.*, vol. 43, pp. 1058–1066, Nov. 1994.
- [6] K. R. Schaubach and N. J. Davis IV, "Microcellular radio-channel propagation prediction," *IEEE Antennas Propagat. Mag.*, pp. 25–34, Aug. 1994.
- [7] K. Rizk, J.-F. Wagen, and F. Gardiol, "Two-dimensional ray-tracing modeling for propagation prediction in microcellular environments," *IEEE Trans. Veh. Technol.*, vol. 46, pp. 508–518, May 1997.
- [8] V. Erceg, S. J. Fortune, J. Ling, A. J. Rustako, and R. A. Valenzuela, "Comparisons of a computer-based propagation prediction tool with experimental data collected in urban microcellular environments," *IEEE J. Select. Areas Commun.*, vol. 15, pp. 677–684, May 1997.
- [9] G. Liang and H. L. Bertoni, "Review of ray modeling techniques for site specific propagation prediction," *Wireless Communications, TDMA Versus CDMA*, 1997.
- [10] G. E. Athanasiadou, A. R. Nix, and J. P. McGeehan, "A ray tracing algorithm for microcellular and indoor propagation modeling," in *IEE ICAP*, Holland, April 4–7, 1995, pp. 2.231–2.235.
- [11] G. E. Athanasiadou, A. R. Nix, and J. P. McGeehan, "A ray tracing algorithm for microcellular wideband propagation modeling," in *IEEE VTC*, Chicago, July 1995, pp. 25–28.
- [12] G. V. Tsoulos, G. E. Athanasiadou, M. A. Beach, and S. C. Swales, "Adaptive antennas for microcellular and mixed cell environments with DS-CDMA," in *Wireless Personal Communications Journal*. Norwell, MA: Kluwer, Aug. 1998, vol. 7, pp. 147–169.
- [13] C. A. Balanis, *Advanced Engineering Electromagnetics*. New York: Wiley, 1989.
- [14] J. B. Keller, "Geometrical theory of diffraction," *J. Opt. Soc. Amer.*, vol. 52, pp. 116–130, Feb. 1962.
- [15] R. G. Kouyoumjian and P. H. Pathak, "A uniform geometric theory of diffraction for an edge on a perfectly conducting surface," *Proc. IEEE*, vol. 62, pp. 1448–1461, Nov. 1974.
- [16] R. J. Luebbers, "Finite conductivity uniform GTD versus knife edge diffraction in prediction of propagation path loss," *IEEE Trans. Antennas Propagat.*, vol. AP-32, pp. 70–76, Jan. 1984.
- [17] H. Bach, *Modern Topics in Electromagnetics and Antennas*. Stevenage, U.K.: Peregrinus Ltd., 1977, ch. 5.
- [18] G. L. Turin *et al.*, "A statistical model for urban multipath propagation," *IEEE Trans. Veh. Technol.*, vol. VT-21, pp. 1–9, Feb. 1972.
- [19] S. Y. Seidel and T. S. Rappaport, "Site-specific propagation prediction for wireless in-building personal communications system design," *IEEE Trans. Veh. Technol.*, vol. 43, pp. 1058–1066, Nov. 1994.

- [20] S. J. Fortune, D. M. Gay, B. W. Kernigham, O. Landron, R. A. Valenzuela, and M. H. Wright, "WISE design of indoor wireless systems: Practical computation and optimization," *IEEE Comp. Sci. and Eng.*, pp. 58–68, Spring 1995.
- [21] G. E. Athanasiadou, A. R. Nix, and J. P. McGeehan, "Investigation into the sensitivity of a microcellular ray-tracing model and comparison of the predictions with narrow-band measurements," in *IEEE VTC*, Ottawa, Canada, May 18–21, 1998, pp. 870–874.
- [22] S. A. Meade, A. R. Nix, and M. A. Beach, "Summary of the processing of the narrowband measurement data for microcells," Tech. Rep. for the BT VURI Project, Aug. 1996.
- [23] T. Schilling, *Principles of Communication Systems*, 2nd ed. New York: McGraw-Hill, 1986.
- [24] R. A. Valenzuela, O. Landron, and D. L. Jacobs, "Estimating local mean signal strength of indoor multipath propagation," *IEEE Trans. Veh. Technol.*, vol. 46, pp. 203–210, Feb. 1997.
- [25] C. Simmonds and M. A. Beach, "Network planning aspects of DS-CDMA with particular emphasis on soft handoff," in *IEEE VTC*, NJ, May 18–20, 1993, pp. 846–849.



**Georgia E. Athanasiadou** received the M.S. degree in electrical and computer engineering from the National Technical University of Athens, Greece, in 1992, and the Ph.D. degree from the University of Bristol, Bristol, U.K., in 1997.

Since 1993, she has been with the Centre for Communications Research of the University of Bristol, working in the area of radio propagation modeling. As part of her research, she has developed, investigated, and evaluated novel indoor and outdoor ray tracing propagation models. She is currently a Research Fellow at the University of Bristol and her research interests, apart from radio propagation, include cell planning and optimization issues with ray tracing models for different air interface techniques, with particular emphasis to adaptive antennas and future generation systems.

Dr. Athanasiadou has been a member of the Technical Chamber of Greece since 1992.

**Andrew R. Nix** received the B.Eng. and Ph.D. degrees in electrical and electronic engineering from the University of Bristol, Bristol, U.K., in 1989 and 1993, respectively.

He joined the academic staff at the University of Bristol in 1993 and was involved in several European funded wireless LAN projects. His current research interests include modulation theory, equalizers, propagation modeling, and high-speed wireless LAN technologies.

**Joseph P. McGeehan** received the B.Eng. and Ph.D. degrees in electrical and electronic engineering from the University of Liverpool, Liverpool, U.K., in 1967 and 1971, respectively.

In November 1984, he was appointed to the Chair of Communications Engineering at the University of Bristol, Bristol, U.K., where he is presently Dean of the Faculty of Engineering.

Prof. McGeehan is a Fellow of the IEE, the Royal Academy of Engineering, and the Royal Society of Arts and Commerce and serves on numerous national and international committees concerned with mobile communications. He was awarded a U.K. Engineering and Physical Sciences Research Grant in 1988 to initiate research on the area of adaptive antennas in cellular systems, work which resulted in an IEEE TRANSACTIONS ON VEHICULAR TECHNOLOGY Award for best paper (N. Shepherd).